INTERNATIONAL JOURNAL FOR NUMERICAL METHODS IN FLUIDS, VOL. 17, 567–587 (1993)

UNSTEADY SUPERSONIC FLOW OVER AN OSCILLATORY AEROFOIL USING A SECOND-ORDER TVD SCHEME

JAE-SOO KIM*

Space R & D Division, Korea Aerospace Research Institute, Daeduck Science Town, P.O. Box 15, Taejeon, 305-606, Korea

SUMMARY

The unsteady flow over an oscillatory NACA0012 aerofoil has been simulated by the calculation with Euler equations. The equations are discretized by an implicit Euler in time, and a second-order space-accurate TVD scheme based on flux vector splitting with van Leer's limiter. Modified eigenvalues are proposed to overcome the slope discontinuities of split eigenvalues at Mach = 0·0 and ±1·0, and to generate a bow shock in front of the aerofoil. A moving grid system around the aerofoil is generated by Sorenson's boundary fitted co-ordinates for each time step. The calculations have been done for two angles of attack $\theta = 5{\cdot}0^\circ \sin(\omega t)$ and $\theta = 3{\cdot}0^\circ + 3{\cdot}0^\circ \sin(\omega t)$ for the free-stream Mach numbers 2·0 and 3·0. The results show that pressure and Mach cells flow along characteristic lines. To examine unsteady effects, the responses of wall pressure and normal force coefficients are analysed by a Fourier series expansion.

KEY WORDS Unsteady supersonic flow Flux vector splitting TVD scheme with limiters Pressure and Mach cells

1. INTRODUCTION

The unsteady flows over a moving aerofoil have received considerable attention for flutter calculations. The potential equation has been widely used for the unsteady transonic flows, e.g. in Ballhaus and Goorjian.[1] Recently, many computations based on the Euler equations have been performed for the transonic and supersonic flows, because of the assumption of irrotational flow behind the potential equation and the lack of Navier-Stokes equations for turbulence model. The unsteady Euler equations have been solved for transonic flows by Magnus and Yoshihara,[2] Steger[3] and Venkatakrishnan and Jameson.[4]

Many numerical schemes for the Euler equations have been developed to get sharp approximations to shocks and contact discontinuities without numerical instabilities. The methods based on central space discretizations use second-order and fourth-order artificial dissipation terms to damp the numerical instability generated from discontinuities and to preserve the Total Variation Diminishing (TVD) property.[4] However, the methods require a procedure to find the optimal coefficients of the artificial dissipation terms for each flow condition. The coefficients become larger as shock becomes stronger. Therefore, the methods are unsuitable for the approximation of unsteady supersonic flows, because the artificial viscosity weakens the unsteady quality of the equations.

Because of these limitations upwind schemes have been developed to consider the physical propagation of a perturbation along characteristics into numerical discretized versions of the Euler equations. A variety of approaches have been tried, such as flux vector splitting by

* Senior Researcher.

0271–2091/93/190567–21$15.50

Received April 1992
Revised April 1993

Steger and Warming[5] and van Leer,[6] and flux difference splitting by Bell *et al.*,[7] Osher and Chakravarthy[8] and Roe.[9] Steger and Warming[5] split flux vectors under the assumption that the flux vectors are homogeneous function of degree one in the vector of conservative variables.

This method might produce a glitch near the sonic point due to eigenvalue switching. Because of these discontinuities, van Leer[6] developed slope-continuous flux vectors, and Liang and Chan[10] introduced a smooth function to avoid the sonic-line glitch. For the flux difference splitting, Bell *et al.*[7] used exact Riemann solutions, and Osher and Chakravarthy[8] and Roe[9] used approximated Riemann solutions. Most of these methods introduce numerical dissipation terms to consider the physical propagation of a perturbation. These dissipation terms might affect the results in the region of discontinuities and viscous layer. Simpson and Whitfield[11] and van Leer *et al.*[12] have compared these schemes. Although the first-order discretizations of these methods can be successfully applied to supersonic flows, the second-order accurate discretizations generate numerical instabilities in the vicinity of discontinuities. Because of these instabilities, flux limiters are introduced to preserve the TVD property in the space discretizations of flux splitting methods. The main property of a TVD scheme is that, unlike monotone scheme, it can be second-order accurate and is oscillation free across discontinuities. In Yee,[13] a wider group of limiters is represented and summarized in a general and simple form. Yee *et al.*[14] extended this TVD scheme to hypersonic flow. The accuracy of these second-order TVD schemes is of lower-order in the vicinity of discontinuities, although second-order accuracy is preserved in the smooth region of flow, where the flow variable can be considered to be continuous. However, most of these schemes have been applied to fixed body or steady-state problems.

In this paper, an upwind scheme with flux vector splitting, LU factorization and flux limiters are applied to the unsteady Euler equations over a moving body. Because of the slope discontinuities of split eigenvalues in the procedure of flux vector splitting, the results obtained with the flux vector splitting method of $\lambda^{\pm}=(\lambda \pm |\lambda|)/2$ have glitches at Mach $=0{\cdot}0$ and $\pm 1{\cdot}0$. The method based on upwind differences has a weakness for the generation of a bow shock in front of the aerofoil. The downstream information of the aerofoil must be propagated upstream to generate a bow shock in the procedure of flux vector splitting. In this work, the eigenvalues modified by a smooth function are proposed for the continuous derivatives of split eigenvalues at Mach $=0{\cdot}0$ and $\pm 1{\cdot}0$, and the generation of bow shock. For the far-field boundary condition, free-stream conditions are given in the region of inflow, and numerical characteristic variables are used for the region of outflow. Although the Euler equations do not require the special imposition of the Kutta condition, zero tangential velocity is imposed at the trailing edge because the tangential velocity to the body surface appears at the trailing edge for the numerical error of co-ordinate transformation matrices.

This method is applied to a one-dimensional shock tube and to a shock reflection on the wall for comparison with the exact solutions. The unsteady supersonic flows over an oscillatory NACA0012 aerofoil is also computed. The results show that pressure and Mach cells flow along characteristic lines. Oscillating phase shift and non-linear effects are studied from the analysis of the wall pressure and the normal force coefficients.

2. NUMERICAL FORMULATION

2.1. Governing equation

The unsteady two-dimensional Euler equation of conservative form in the Cartesian co-ordinates is given by

$$\frac{\partial \bar{Q}}{\partial t}+\frac{\partial E(\bar{Q})}{\partial x}+\frac{\partial F(\bar{Q})}{\partial y}=0, \tag{1}$$

where $\bar{Q}$, $E(\bar{Q})$ and $F(\bar{Q})$ are column vectors non-dimensionalized by free-stream sound velocity (C_0), characteristic length (L) and free-stream density (ρ_0). By a generalized co-ordinate system of the form $\tau = t$, $\xi = \xi(t, x, y)$ and $\eta = \eta(t, x, y)$, equation (1) can be transformed to

$$\frac{\partial Q}{\partial \tau} + \frac{\partial E(Q)}{\partial \xi} + \frac{\partial F(Q)}{\partial \eta} = 0, \tag{2}$$

where

$$Q = \frac{1}{J}\begin{bmatrix} \rho \\ \rho u \\ \rho v \\ e \end{bmatrix}, \quad E = \frac{1}{J}\begin{bmatrix} \rho U \\ \rho u U + \xi_x P \\ \rho v U + \xi_y P \\ (e+P)U - \xi_t P \end{bmatrix}, \quad F = \frac{1}{J}\begin{bmatrix} \rho V \\ \rho u V + \eta_x P \\ \rho v V + \eta_y P \\ (e+P)V - \eta_t P \end{bmatrix},$$

where ρ, (u, v), P and e are density, Cartesian velocity components, pressure and total energy per unit volume, respectively. J represents the Jacobian of the transformation, while ξ_x, ξ_y, ... represent transformation matrices. U and V are the contravariant components defined as $U = \xi_t + u\xi_x + v\xi_y$ and $V = \eta_t + u\eta_x + v\eta_y$.

2.2. *Time-discretization*

For time-discretization, the increment vectors can be defined by $\Delta Q = Q_{n+1} - Q_n$, $\Delta E = E_{n+1} - E_n$, and $\Delta F = F_{n+1} - F_n$. The increment flux vectors ΔE and ΔF can be written as

$$\Delta E = \frac{\partial E}{\partial Q}\Delta Q = A\Delta Q,$$

$$\Delta F = \frac{\partial F}{\partial Q}\Delta Q = B\Delta Q, \tag{3}$$

where A and B are the Jacobian matrices of E and F, respectively. By using the increment vectors and the Jacobian matrices, equation (2) can be written in the form of a non-iterative implicit backward Euler finite difference equation as

$$[I + \Delta t(\delta_\xi A + \delta_\eta B)]\Delta Q = -\Delta t[\delta_\xi E + \delta_\eta F], \tag{4}$$

where I is the identity matrix and δ is an approximate spatial difference operator.

2.3. *Flux vector splitting*

Before the space discretization, the flux vectors and the Jacobian matrices are split to consider the physical propagation of a wave along characteristics. The eigenmatrices of A and B are given as the following diagonal matrices:[15]

$$\begin{aligned} \Lambda_\xi &= D[U, U, U + C(\xi x^2 + \xi y^2)^{1/2}, U - C(\xi x^2 + \xi y^2)^{1/2}], \\ \Lambda_\eta &= D[V, V, V + C(\eta x^2 + \eta y^2)^{1/2}, V - C(\eta x^2 + \eta y^2)^{1/2}], \end{aligned} \tag{5}$$

where C is the sound velocity and D is a diagonal matrix.

When the eigenvalues are split by $\lambda^{\pm} = (\lambda \pm |\lambda|)/2$, they have slope discontinuities at Mach = 0·0 and $\pm$1·0. The discontinuities generate glitches in the solution at sonic points, because the eigenvalue is either suddenly set to zero or is suddenly non-zero. This means that the exchange of information of wave propagation is not enough in the vicinity of Mach = 0·0 and $\pm$1·0. In order to overcome this problem, van Leer[6] developed slope-continuous flux vectors, and Liang and Chan[10] introduced a smooth function.

In this paper, the eigenvalues are split into two slope continuous values by the introduction of an additional function:

$$\lambda_i^{\pm} = \frac{\lambda_i \pm |\lambda_i|}{2} \pm \varepsilon(\alpha),$$
$$\varepsilon(\alpha) = \frac{C}{4\varepsilon_0}\alpha^2 - \frac{C}{2}\alpha + \frac{C}{4}\varepsilon_0, \tag{6}$$

where $\alpha = M-1$, M or $M+1$ ($|\alpha| \leqslant \varepsilon_0$). Because the sudden cut-off of wave propagation can be prevented by the modified eigenvalue splitting, smooth transitions can be obtained at sonic points. The modified eigenvalues of $\lambda_{1,2}^{\pm}$ are plotted in Figure 1. The eigenvalues are smoothly changed, and they can consider the downwind characteristics around $M = 0{\cdot}0$. These modified eigenvalues are important for the generation of a bow shock in front of the aerofoil. The information of the aerofoil must be propagated upstream for the generation of a bow shock. However, the split eigenvalue without the additional function cannot approximate the wave propagation from the aerofoil, because negative eigenvalues are set to zero. As described earlier, various splitting techniques have been proposed. These kind of techniques can be unstable because of downwind characteristics. Therefore, although the value of $\varepsilon(\alpha)$ must be large enough in the vicinity of the sonic points and the aerofoil so that wave propagates into the downwind direction, it must be small in the other regions.

The Jacobian matrices are split by the transformation matrix T and its inverse T^{-1} (see Reference 15) with the split eigenvectors:

$$\begin{aligned} A &= T_\xi \Lambda_\xi T_\xi^{-1} = T_\xi(\Lambda_\xi^+ + \Lambda_\xi^-)T_\xi^{-1} \\ &= T_\xi \Lambda_\xi^+ T_\xi^{-1} + T_\xi \Lambda_\xi^- T_\xi^{-1} = A^+ + A^-, \\ B &= T_\eta \Lambda_\eta T_\eta^{-1} = T_\eta(\Lambda_\eta^+ + \Lambda_\eta^-)T_\eta^{-1} \\ &= T_\eta \Lambda_\eta^+ T_\eta^{-1} + T_\eta \Lambda_\eta^- T_\eta^{-1} = B^+ + B^-. \end{aligned} \tag{7}$$

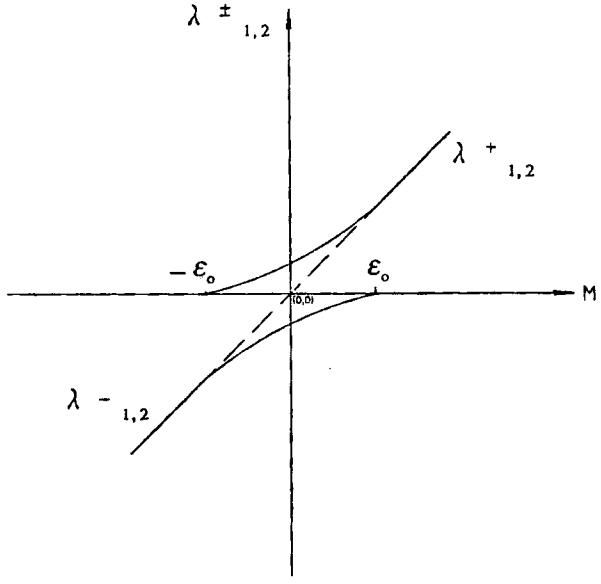

Figure 1. Split eigenvalues of $\lambda_{1,2}^{\pm}$

Because the flux vectors E and F are homogeneous (of degree one) functions of Q, they are split as

$$E = AQ = (A^+ + A^-)Q = A^+Q + A^-Q = E^+ + E^-, \tag{8}$$
$$F = BQ = (B^+ + B^-)Q = B^+Q + B^-Q = F^+ + F^-.$$

2.4. Space discretization

With the use of the split flux vectors and matrices, equation (4) can be written as an upwind difference equation:

$$[I + \Delta t(\delta_\xi^- A^+ + \delta_\xi^+ A^- + \delta_\eta^- B^+ + \delta_\eta^+ B^-)]\Delta Q = -\Delta t(\delta_\xi^- E^+ + \delta_\xi^+ E^- + \delta_\eta^- F^+ + \delta_\eta^+ F^-) = \text{RHS}, \tag{9}$$

where δ^+ represents a forward space difference operator, and δ^- represents a backward operator. The terms on the right-hand side are discretized by a second-order-accurate upwind formulation with flux limiters, and the terms on the left-hand side are discretized by a first-order-accurate formulation. However, since the operator on the LHS represents the difference of increment vectors, equation (9) can preserve second-order accuracy with the assumption of the same order of $\Delta\xi$, $\Delta\eta$ and Δt.

For example, Jacobian metrics $A^\pm$ and flux vectors $E^\pm$ can be discretized:

$$\begin{aligned}
&\delta_\xi^- A^+ = A_i^+ - A_{i-1}^+, \\
&\delta_\xi^+ A^- = A_{i+1}^- - A_i^-, \\
&\delta_\xi^- E^+ = (1 + \tfrac{1}{2}\psi_{i-1/2}^+)E_i^+ - (1 + \tfrac{1}{2}\psi_{i-1/2}^+ + \tfrac{1}{2}\psi_{i-3/2}^+)E_{i-1}^+ + \tfrac{1}{2}\psi_{i-3/2}^+ E_{i-2}^+, \\
&\delta_\xi^+ E^- = -\{(1 + \tfrac{1}{2}\psi_{i+1/2}^-)E_i^- - (1 + \tfrac{1}{2}\psi_{i+1/2}^- + \tfrac{1}{2}\psi_{i+3/2}^-)E_{i+1}^- + \tfrac{1}{2}\psi_{i+3/2}^- E_{i+2}^-\},
\end{aligned} \tag{10}$$

where $\psi^\pm$ are limiters.

2.5. Limiter

An upwind algorithm with first-order numerical flux is a monotonic scheme and, hence, a TVD scheme. However, the straightforward replacement of a first-order numerical flux by an appropriate second-order accurate flux leads to the generation of unstable solutions around discontinuities, similar to those encountered with a central scheme. To overcome this limitation, non-linear limiters have been proposed to restrict the amplitude of the gradients appearing in the additional terms of the second-order numerical flux, such as Minmod of van Leer, Superbee of Roe and the work of Osher's.[16] These limiters ensure the TVD condition of the schemes. Although each kind of limiter has its own characteristics, the accuracy of the schemes are of second-order in the smooth region of flow, where the flow variables can be considered to be continuous, and of lower-order in the vicinity of the discontinuities.

In this paper, van Leer's limiter is used, which is defined by

$$\psi^\pm = (\gamma^\pm + |\gamma^\pm|)/(1 + \gamma^\pm), \tag{11}$$

where

$$\gamma_{i+1/2}^+ = \frac{E_{i+2}^+ - E_{i+1}^+}{E_{i+1}^+ - E_i^+}, \qquad \gamma_{i+1/2}^- = \frac{E_i^- - E_{i-1}^-}{E_{i+1}^- - E_i^-}.$$

2.6. LU-factorization

The LU-factorization technique is used to invert equation (9). For the periodic condition of the O-grid system equation (9) is written as equation (12a) and for the H-grid or C-grid system it is

written as in (12b)

$$[I+\Delta t(\delta_\xi^- A^+ + \delta_\xi^+ A^- + \delta_\eta^- B^+)]\,[I+\Delta t(\delta_\eta^+ B^-)]\Delta Q = \text{RHS}, \tag{12a}$$

$$[I+\Delta t(\delta_\xi^- A^+ + \delta_\eta^- B^+)]\,[I+\Delta t(\delta_\xi^+ A^- + \delta_\eta^+ B^-)]\Delta Q = \text{RHS}. \tag{12b}$$

This can be solved by two sweeps through the mesh. The two sweeps of equation (12a) are

$$\begin{aligned}[I+\Delta t(\delta_\xi^- A^+ + \delta_\xi^+ A^- + \delta_\eta^- B^+)]\overline{\Delta Q} &= \text{RHS},\\ [I+\Delta t(\delta_\eta^+ B^-)]\Delta Q &= \overline{\Delta Q}.\end{aligned} \tag{13}$$

Similar sweeps are applied to equation (12b).

2.7. *Boundary condition*

For the far-field boundary, the characteristic values are used for the region of outflow, and the free-stream condition for the region of inflow. Along the body surface $\eta(t, x, y)=0$, the condition that the velocities normal to the body surface are zero is given by

$$\begin{aligned}u &= \frac{1}{J}\{\eta_y(U-\xi_t)+\xi_y\eta_t\},\\ v &= \frac{1}{J}\{-\eta_x(U-\xi_t)-\xi_x\eta_t\}.\end{aligned} \tag{14}$$

The pressure on the body surface can be obtained from the normal momentum equation:

$$(\xi_x\eta_x+\xi_y\eta_y)P_\xi+(\eta_x^2+\eta_y^2)P_\eta=\rho(\partial_\tau\eta_t+u\partial_\tau\eta_x+v\partial_\tau\eta_y)-\rho U(\eta_x u_\xi+\eta_y v_\xi) \tag{15}$$

where ρ and U are extrapolated from interior points. For the trailing edge, it is known that Euler computation does not require the special imposition of the Kutta condition. However, the velocity tangential to the body surface exists because of the numerical error of the co-ordinate transformation matrices. Then, the tangential velocity is set to zero at the trailing edge, which means that the trailing edge is imposed as a stagnation point of the contravariant velocity field.

3. RESULTS AND DISCUSSION

3.1. *Shock tube problem*

Calculation is performed for a shock tube problem with $P_L=10^5$, $\rho_L=1$, $P_R=10^4$, $\rho_R=0{\cdot}125$ and $U_L=U_R=0$, where L and R represent the left and right sides, respectively. This problem has been tested by various schemes for comparison with the exact solution.[16] The results of the first-order upwind scheme at $t=6{\cdot}2$ msec are shown in Figure 2 along with the exact solution. Figure 3, with van Leer's limiter, shows a sharp approximation to the exact solutions.

For the effect of the eigenvalues modified by a smooth function, another problem for the flow with $P_L=10^5$, $\rho_L=1$, $P_R=10^3$, $\rho_R=0{\cdot}01$ and $U_L=U_R=0$ at $t=3{\cdot}9$ msec is considered. The results by the eigenvalues without the smooth function in Figure 4 have glitches in the vicinity of sonic point, but they are smoothed in Figure 5 by the modified eigenvalues.

3.2. *Shock reflection on the wall*

The shock reflection problem shown in Figure 6 is solved to examine the characteristics of shock reflection. Figures 7(a) and 7(b) show the contour lines of the pressure of the first-order and

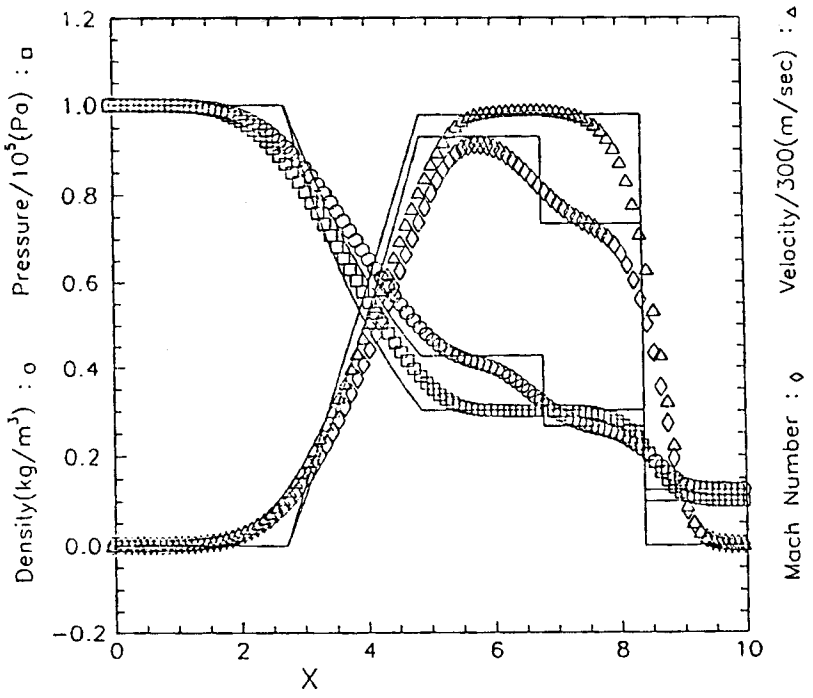

Figure 2. Results of first-order scheme ($P_L = 10^5$, $\rho_L = 1$, $P_R = 10^4$, $\rho_R = 0{\cdot}125$, $U_L = U_R = 0$)

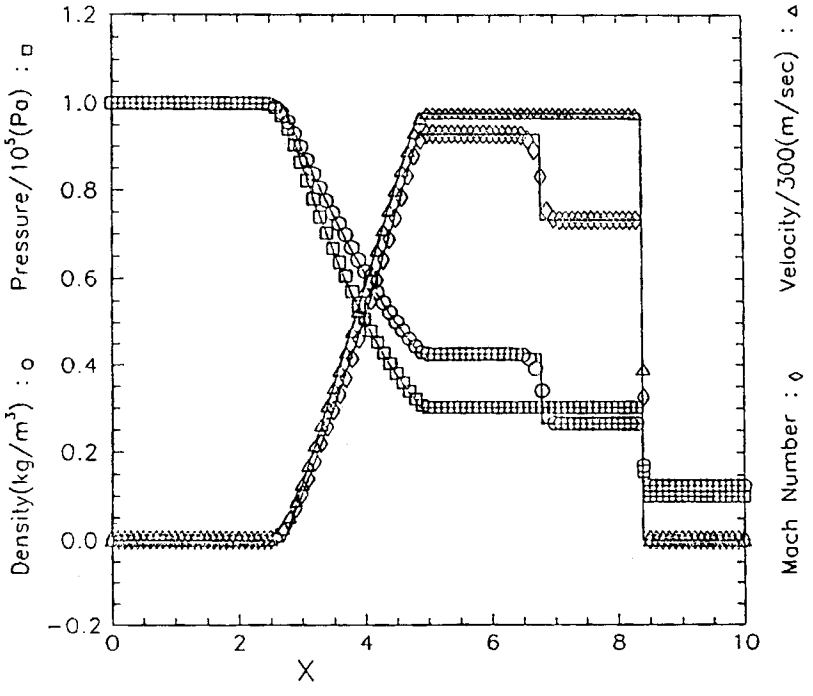

Figure 3. Results of second-order scheme ($P_L = 10^5$, $\rho_L = 1$, $P_R = 10^4$, $\rho_R = 0{\cdot}125$, $U_L = U_R = 0$)

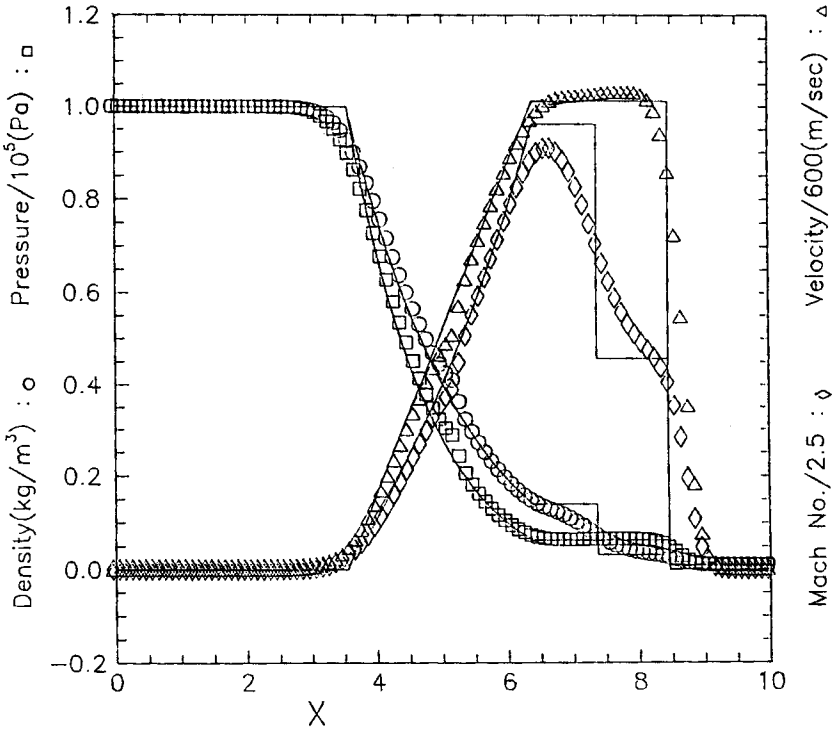

Figure 4. Results by the eigenvalues without the smooth function ($P_L = 10^5$, $\rho_L = 1$, $P_R = 10^3$, $\rho_R = 0{\cdot}01$, $U_L = U_R = 0$)

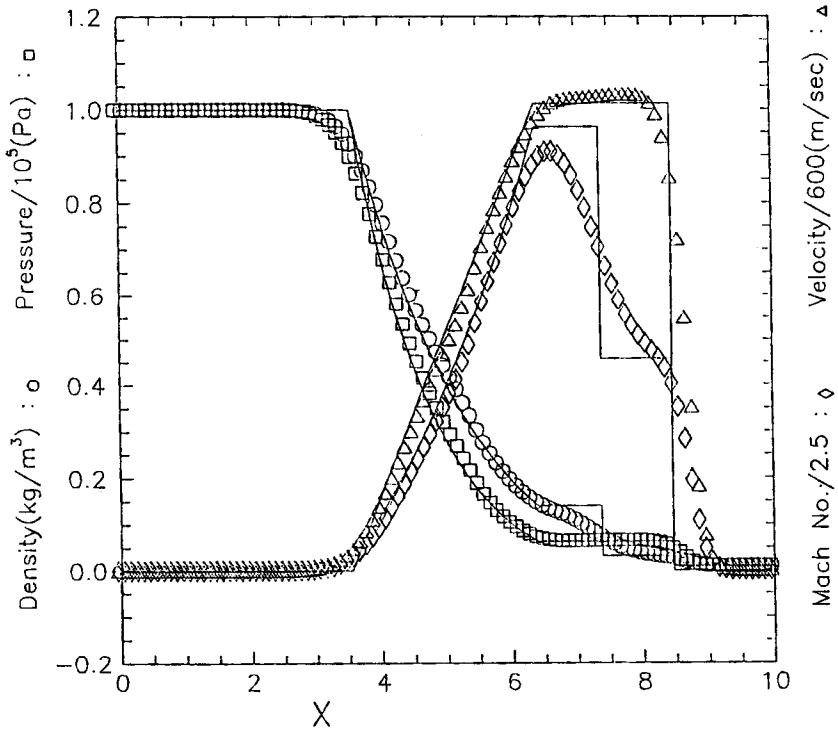

Figure 5. Results by the eigenvalues with the smooth function ($P_L = 10^5$, $\rho_L = 1$, $P_R = 10^3$, $\rho_R = 0{\cdot}01$, $U_L = U_R = 0$)

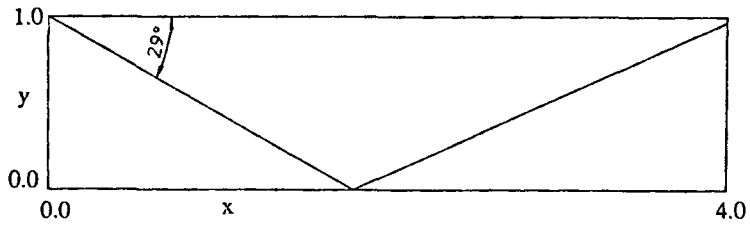

Figure 6. Geometry of shock reflection on the wall $(\rho, u, v, P)_{(0\cdot0, y, t)}=(1, 2\cdot9, 0, 1, 1/4)$, $(\rho, u, v, P)_{(x, 1\cdot0, t)}=(1\cdot69997, 2\cdot61934, -0\cdot50632, 1\cdot52819)$

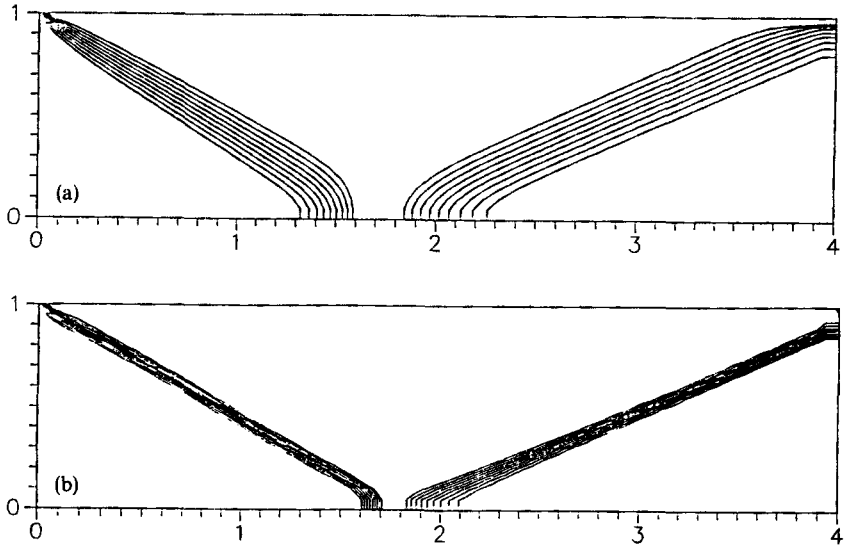

Figure 7. (a) Pressure contour of first-order scheme (b) Pressure contour of second-order scheme

the second-order schemes, respectively, to compare the concentration of lines. The figures show that a distinct shock can be captured by the second-order scheme. For the convergence history from a supersonic initial condition, the history of the residual of the continuity equation is plotted in Figure 8 for the first-order scheme with $\Delta t=0\cdot025$ and $\Delta t=0\cdot05$, and for the second-order scheme with $\Delta t=0\cdot025$. The figure shows that the solutions converge within about 100 or 200 steps. Because the length of the numerical domain x is 4·0, it is expected to take about four seconds of non-dimensional time to propagate the initial disturbed condition to the whole numerical domain.

3.3. Oscillatory NACA0012 aerofoil

The unsteady flow is calculated over an oscillatory NACA0012 aerofoil with the angle of attack of

$$\theta=\theta_m+\theta_0\sin(\omega t), \tag{16}$$

as shown in Figure 9. The O-grid system of 160×61 are generated by Sorenson's method of boundary fitted co-ordinates[17] for each time step. The steady-state solutions are used as an initial

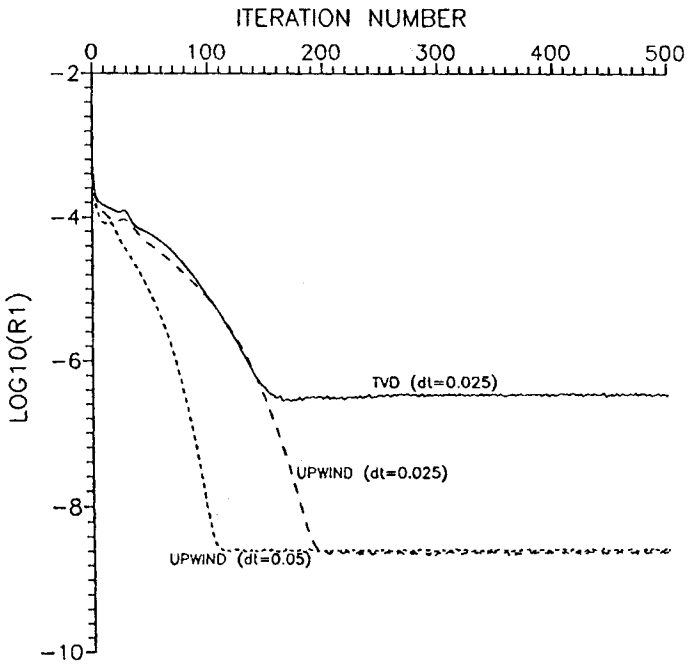

Figure 8. History of numerical residual of the continuity equation

condition to converge to a periodic steady state. The calculations have been performed for two cases of angle of attack (AA) with $\theta_m = 0{\cdot}0°$ and $\theta_0 = 5{\cdot}0°$ (AA I) and $\theta_m = 3{\cdot}0°$ and $\theta_0 = 3{\cdot}0°$ (AA II) in the free stream Mach number of 2·0 and 3·0 with frequencies $\omega = \pi$, 2π, $2{\cdot}5\pi$ and 4π.

The change of the local angle of attack on the body surface (x_b, y_b) of the moving aerofoil can be written as

$$\theta_{body}(x_b, y_b) = \tan^{-1}\left(\frac{U_0 \sin\theta + x_b\dot{\theta}}{U_0 \cos\theta - y_b\dot{\theta}}\right). \tag{17}$$

It can be expected that equation (17) has the characteristics of phase shift and higher-modes of fluctuation with respect to a change in the fixed co-ordinates (x, y). Equation (17) can be expanded as a Fourier-series:

$$\theta_{body}(x_b, y_b) = \theta_m + \theta_1(x_b, y_b)\sin(\omega t + \phi_1) + \theta_2(x_b, y_b)\sin(2\omega t + \phi_2) + \cdots \tag{18}$$

where θ_1 and θ_2 are the first- and second-order fluctuation components of AA, and ϕ_1 and ϕ_2 are their phase angles, respectively. The characteristics of phase shift in the body axes (x_b, y_b) exert a direct influence on the response of wall pressure. The ϕ_1 are plotted in Figure 10 along the body surface for AA I. The variation of ϕ_1 becomes larger as the frequency is increased.

The steady-state pressure contours are plotted in Figure 11 for a free-stream Mach number of 2·0, and an angle of attack of 0·0. The figure shows a bow shock in front of the aerofoil and a weak shock at the trailing edge.[3] The history of the normal force coefficient C_n, as defined by $\int(p - p_0)ds/0{\cdot}5\rho_0 u_0^2$, shows that the solution converges to a periodic steady state within two to three periodic calculations. The history is plotted in Figure 12 for the AAs I and II for $M_0 = 2{\cdot}0$ and $\omega = 2\pi$. For a free-stream Mach number of 2·0, the pressure contours are plotted in Figures

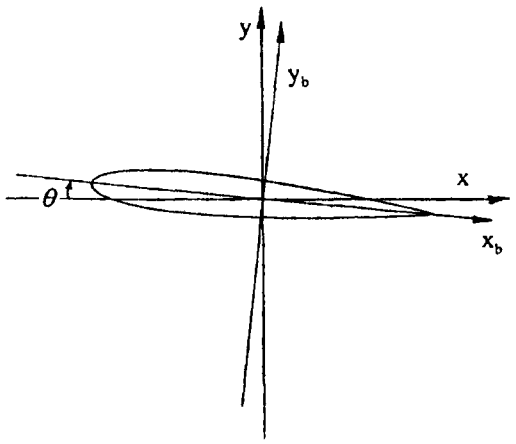

Figure 9. Geometry of oscillatory NACA0012 aerofoil

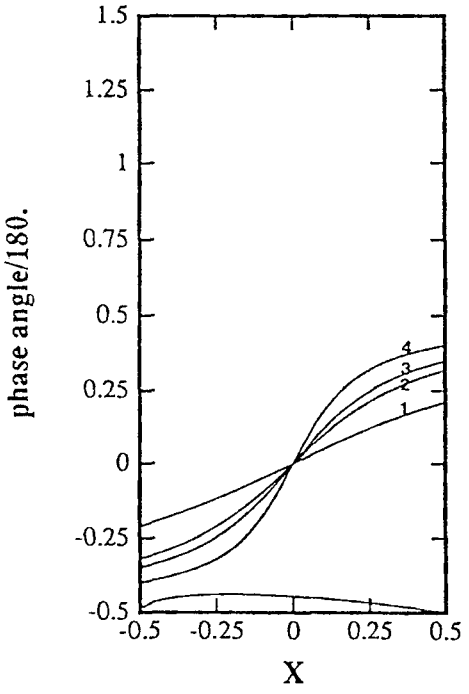

Figure 10. First-mode phase angle ϕ_1 of fluctuation of $\theta_{body}(x_b, y_b)$ for $M_0=2{\cdot}0$: (1) $\omega=\pi$; (2) $\omega=2\pi$; (3) $\omega=2{\cdot}5\pi$; (4) $\omega=4\pi$

13(a) and 13(b) for the AA I with $\omega=2\pi$, and in Figures 14(a) and 14(b) for the AA II with $\omega=4\pi$. The Mach contours are plotted in Figures 15(a) and 15(b) for the AA I with $\omega=4\pi$. For a free-stream Mach number of 3·0, the pressure contours are plotted in Figures 16(a) and 16(b) for the AA II with $\omega=4\pi$. The pressure and Mach cells flow along characteristic lines. The length of

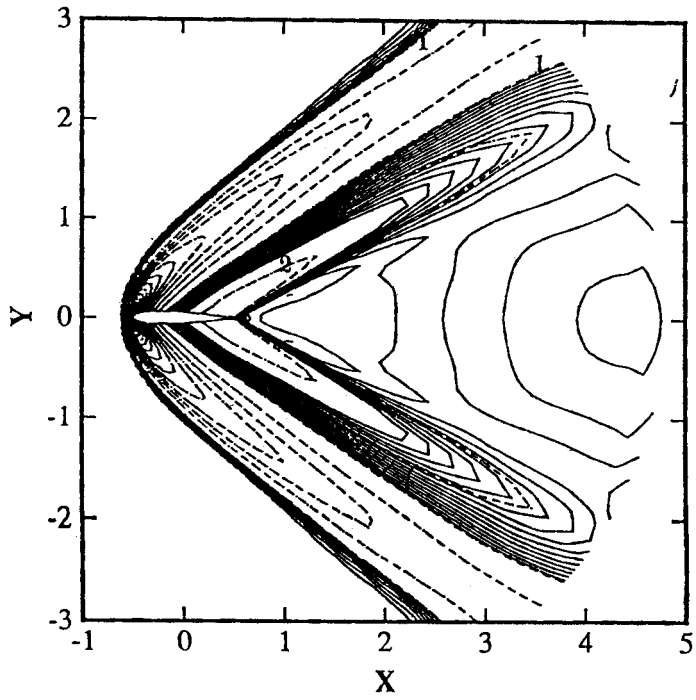

Figure 11. Pressure contour of steady state ($M=2{\cdot}0$, $\theta=0{\cdot}0°$, ΔP (– – –)$=0{\cdot}1$, ΔP (——)$=0{\cdot}01$, point 1: $P=0{\cdot}8$, point 2: $P=0{\cdot}6$)

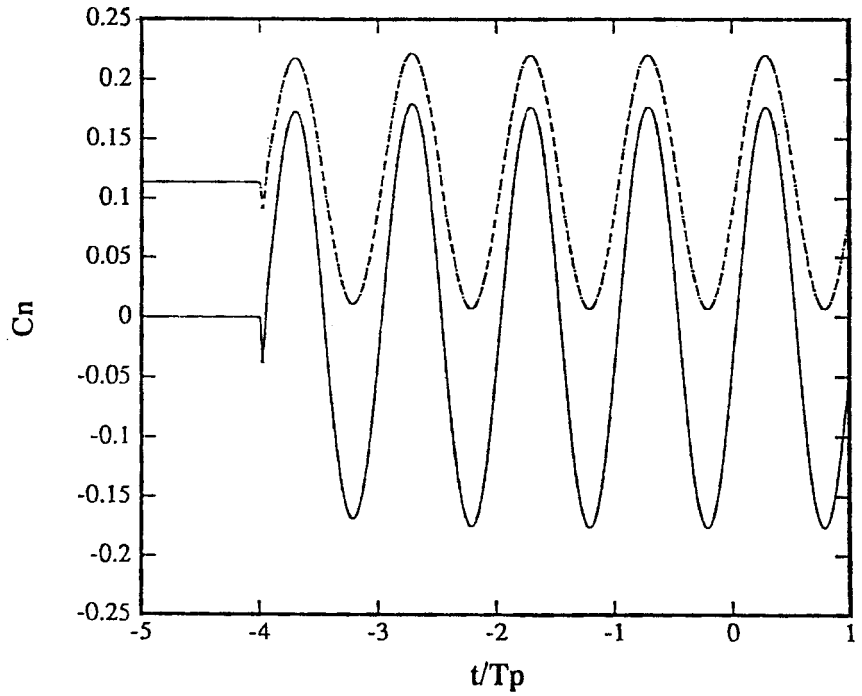

Figure 12. History of normal force coefficient for $M_0=2{\cdot}0$ and $\omega=2\pi$: ——, AA I; – – –, AA II

cells are approximately proportional to the periodic time T_p. The pressure cells are more distinct than the Mach cells. They are rapidly decaying in the case of high Mach number. The oscillatory motion of the aerofoil has little effect on the bow shock in front of the aerofoil.

The pressure coefficient distributions, as defined by $(p-p_0)/0{\cdot}5\rho_0 u_0^2$, on the body surface and symmetric line at $t/T_p=0{\cdot}0$ are plotted in Figure 17 for $M_0=2{\cdot}0$, $\omega=2\pi$ and AA I. Figure 17 shows a strong shock in front of the aerofoil. The pressure at the stagnation point is 4·05 at $t/T_p=0{\cdot}0$. Compared with the stagnation pressure of 4·13 after the normal shock of a steady free stream Mach number of 2·0, it is a very good result. In order to analyse the wall pressure, the pressure can be expanded as a Fourier series.

$$P_{\text{wall}}-P_{\text{steady}}=P_s+P_1\sin(\omega t+\phi_1)+P_2\sin(2\omega t+\phi_2)+\cdots \tag{19}$$

In equation (19), P_s represents a steady value induced by the oscillatory motion, P_1 and P_2 are the first- and second-mode fluctuation components of wall pressure, and ϕ_1 and ϕ_2 are their phase angles, respectively. From the analysis, the first mode of fluctuation is dominant, and the higher-modes are rapidly decaying. P_1 and ϕ_1 are plotted in Figures 18(a) and 18(b). Compared with the phase angles of local angle of attack, the phase angle of first mode has very similar trend. However, the first mode of phase angles of the upper and lower walls have a phase shift of π. With the increase of frequency, the amplitudes of fluctuations and the variations of phase angle become larger. Because the stagnation point is moving in this region, the second mode of fluctuation is more dominant than the first mode. The amplitude in the forward region is larger than the backward region.

In addition, the normal force coefficients are plotted in Figure 19 for $M_0=2{\cdot}0$. They can also be expanded as a Fourier series. The first-mode of fluctuation is also dominant. In Figures 20 and 21, the amplitude C_{n1} and the phase angle ϕ_1 of first-mode fluctuation are plotted. As one can note from Figures 20 and 21, the amplitude increases with the increase in frequency, and it converges to certain values. The phase angles of AA I and II are the same for the same Mach number. This means that the phase angle is strongly dependent on the frequency. It rapidly decreases as frequency increases.

4. CONCLUSION

The Euler equations have been solved for unsteady supersonic flows over an oscillatory NACA0012 aerofoil by an implicit Euler in time, and a second-order space-accurate TVD scheme based on flux vector splitting with van Leer's limiter. The split eigenvalues are applied successfully to overcome slope discontinuities at Mach $=0{\cdot}0$ and $\pm 1{\cdot}0$, and to generate a bow shock in front of the aerofoil. The flows of a free-stream Mach number of 2·0 and 3·0 have been calculated with AA $\theta=5{\cdot}0^\circ\sin(\omega t)$ and $\theta=3{\cdot}0^\circ+3{\cdot}0^\circ\sin(\omega t)$. The results show that pressure and Mach cells flow along characteristic lines. The length of cells are approximately proportional to the periodic time T_p. Compared with the stagnation pressure after normal shock, the result of the pressure at the stagnation point is very good. The wall pressure strongly depends on the change of local AA on the surface in the body axes (x_b, y_b). The normal force coefficients have phase shift angles with respect to AA. The amplitude of fluctuation increases with increase in frequency, and converges to certain values. The phase shift angle is strongly dependent on the frequency, and it rapidly decreases as the frequency increases.

ACKNOWLEDGEMENT

This work was supported by the Basic Research Fund of the Korea Aerospace Research Institute.

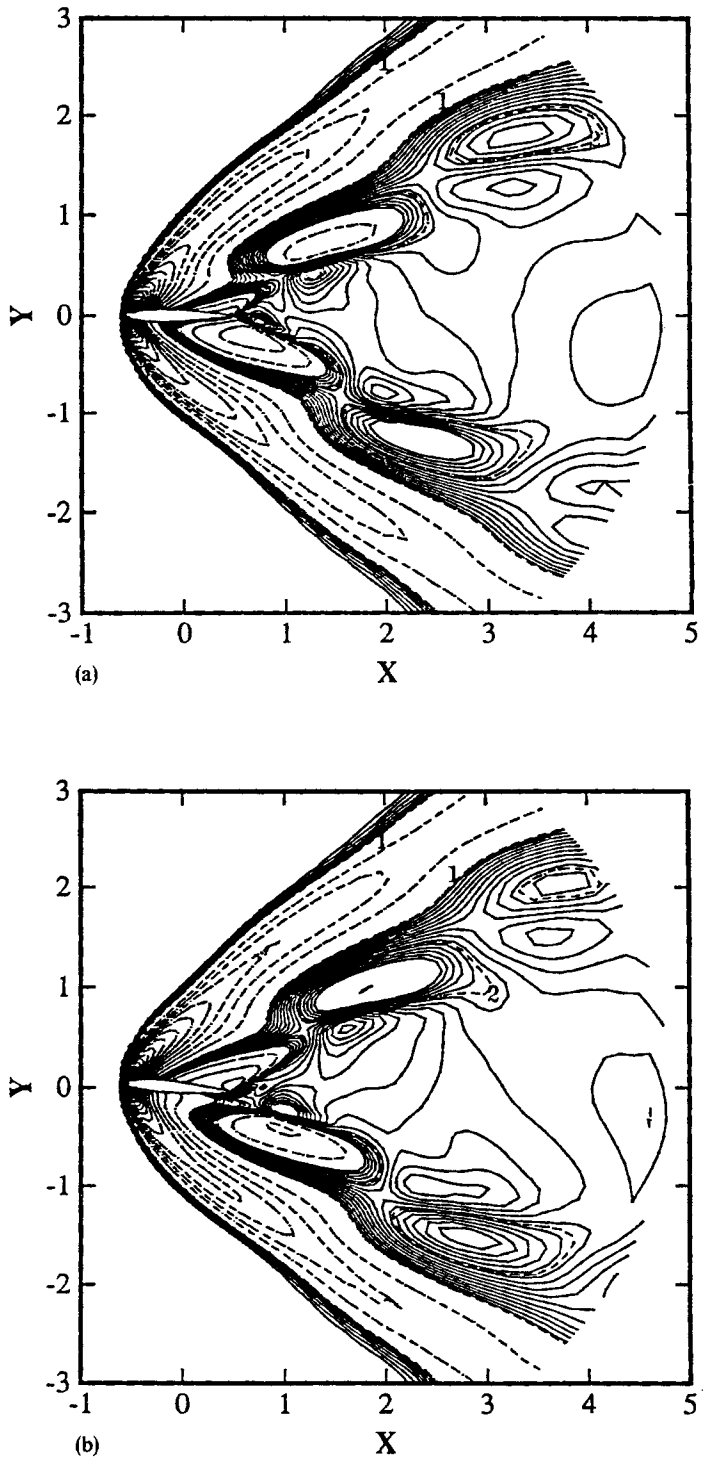

Figure 13. Pressure contours for AA I, $M_0=2{\cdot}0$ and $\omega=2\pi$ (ΔP (– – –)$=0{\cdot}1$, ΔP (——)$=0{\cdot}01$, point 1: $P=0{\cdot}8$, point 2: $P=0{\cdot}7$): (a) $t/T_p=0{\cdot}0$ ($\theta=0{\cdot}0°$); (b) $t/T_p=0{\cdot}25$ ($\theta=5{\cdot}0°$)

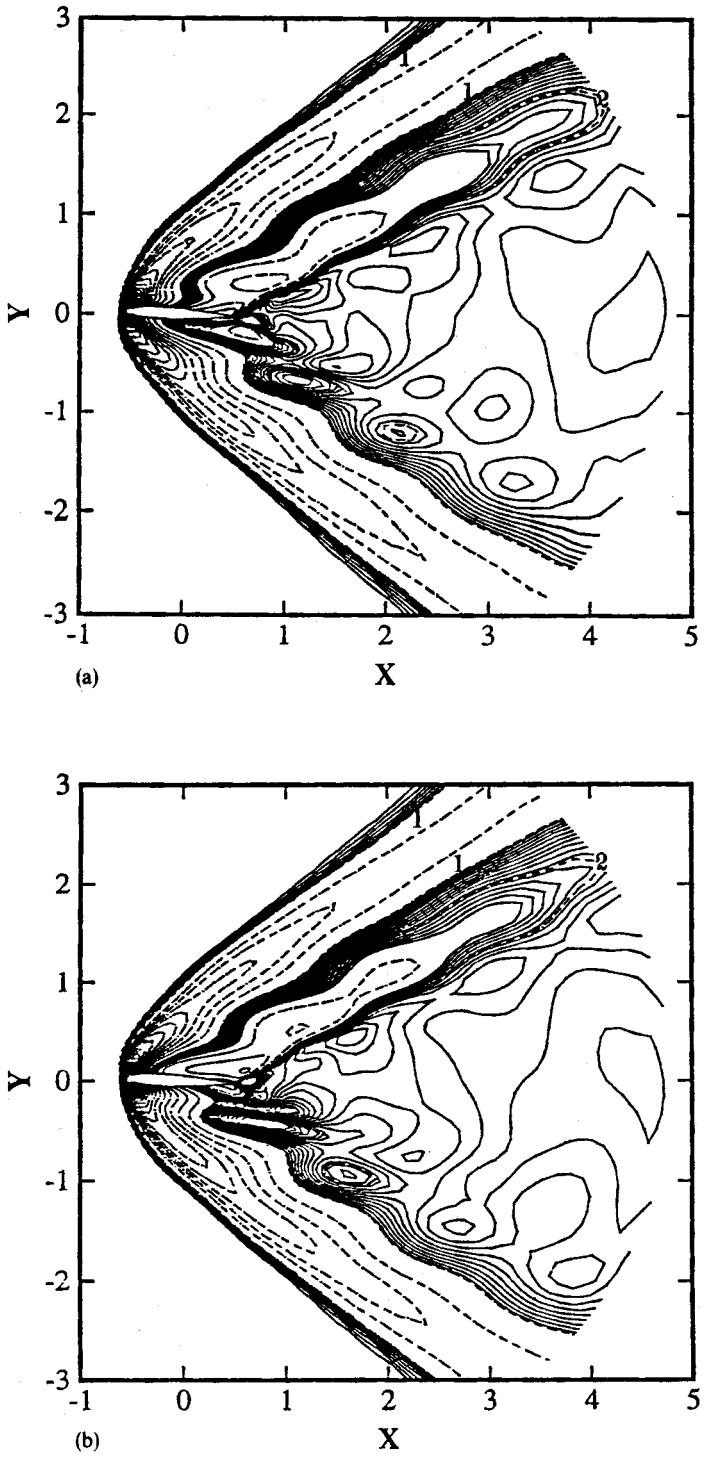

Figure 14. Pressure contours for AA II, $M_0=2{\cdot}0$ and $\omega=4\pi$ (ΔP (– – –)$=0{\cdot}1$, ΔP (——)$=0{\cdot}01$, point 1: $P=0{\cdot}8$, point 2: $P=0{\cdot}7$): (a) $t/T_p=0{\cdot}0$ ($\theta=3{\cdot}0°$); (b) $t/T_p=0{\cdot}5$ ($\theta=3{\cdot}0°$)

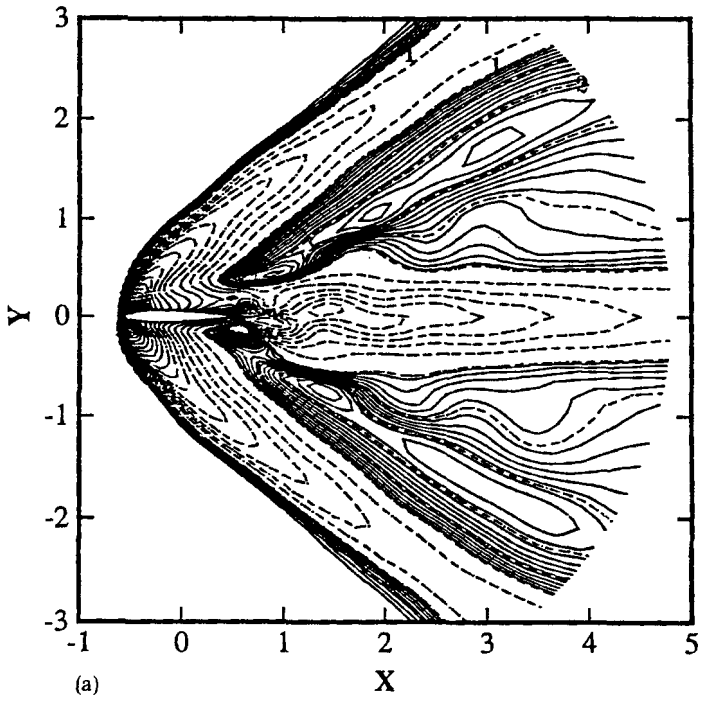

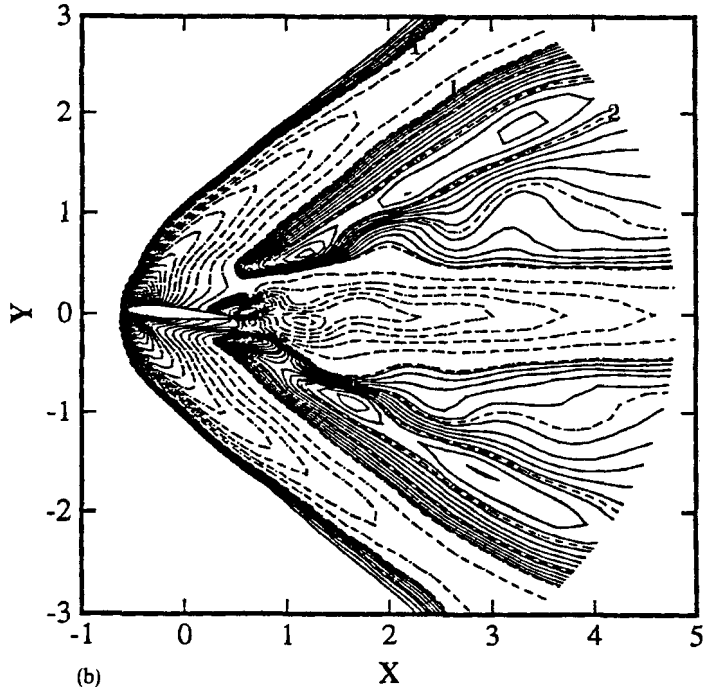

Figure 15. Mach contours for AA I, $M_0 = 2{\cdot}0$ and $\omega = 4\pi$ (ΔM (– – –) $= 0{\cdot}05$, ΔM (——) $= 0{\cdot}01$, point 1: $M = 1{\cdot}9$, point 2: $M = 2{\cdot}0$): (a) $t/T_p = 0{\cdot}0$ ($\theta = 0{\cdot}0°$); (b) $t/T_p = 0{\cdot}25$ ($\theta = 5{\cdot}0°$)

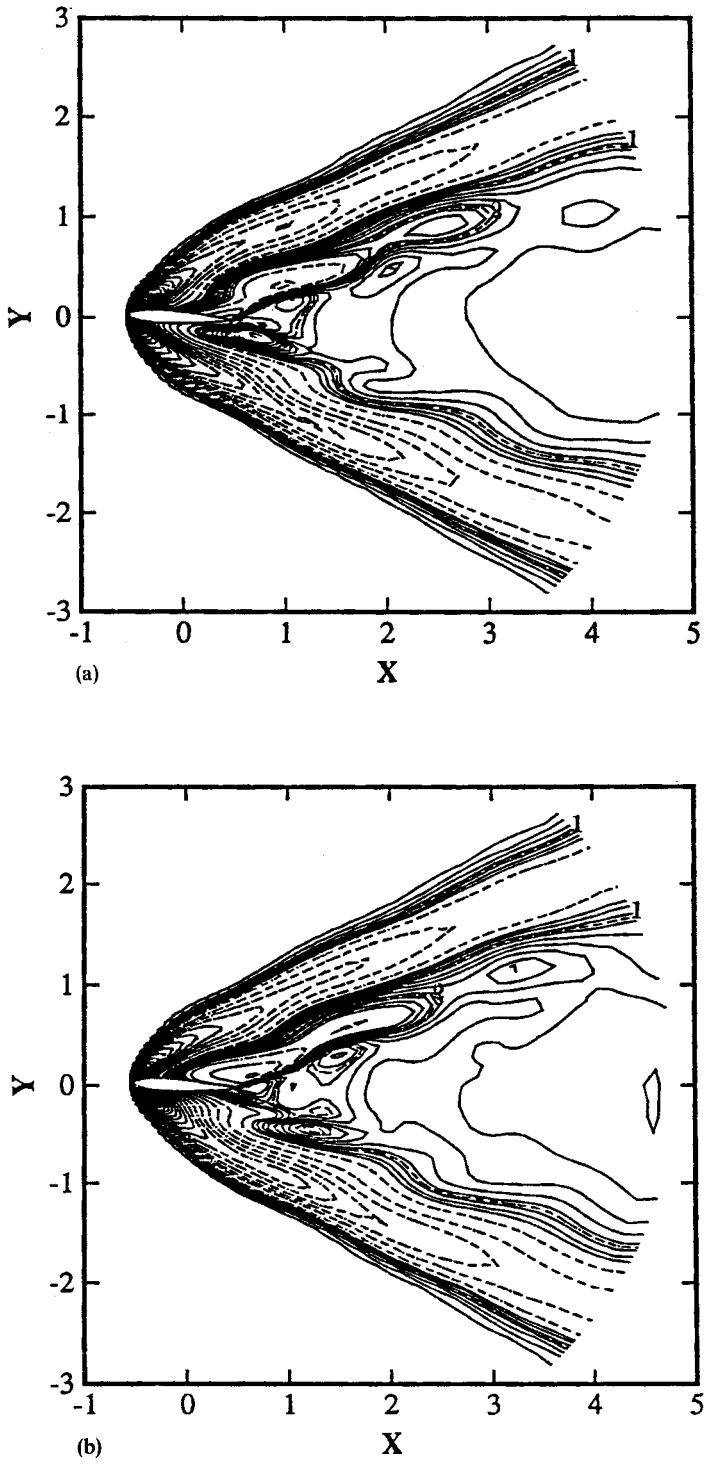

Figure 16. Pressure contours for AA II, $M_0=3{\cdot}0$ and $\omega=4\pi$ (ΔP (----)$=0{\cdot}1$, ΔP (———)$=0{\cdot}02$, point 1: $P=0{\cdot}8$, point 2: $P=0{\cdot}9$): (a) $t/T_p=0{\cdot}0$ ($\theta=3{\cdot}0°$); (b) $t/T_p=0{\cdot}5$ ($\theta=3{\cdot}0°$)

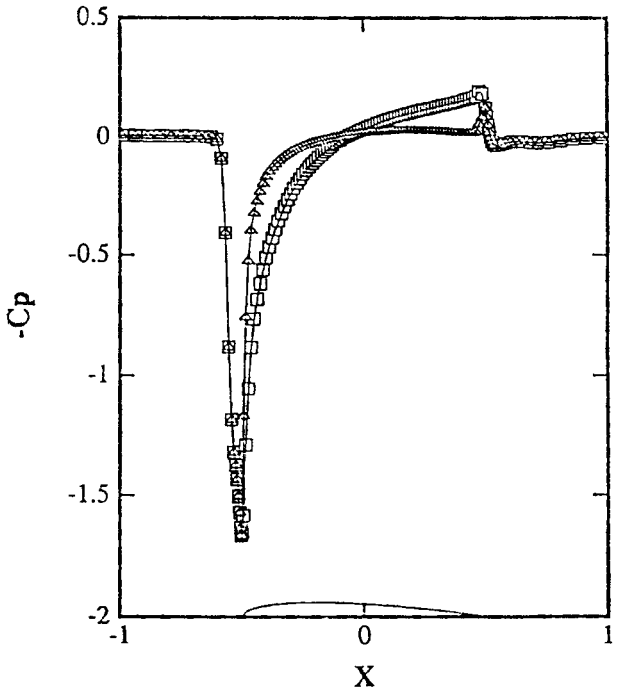

Figure 17. Pressure coefficient distribution on the body surface ($M_0=2{\cdot}0$ and $t/T_p=0{\cdot}0$, —□—, upper wall; —△—, lower wall)

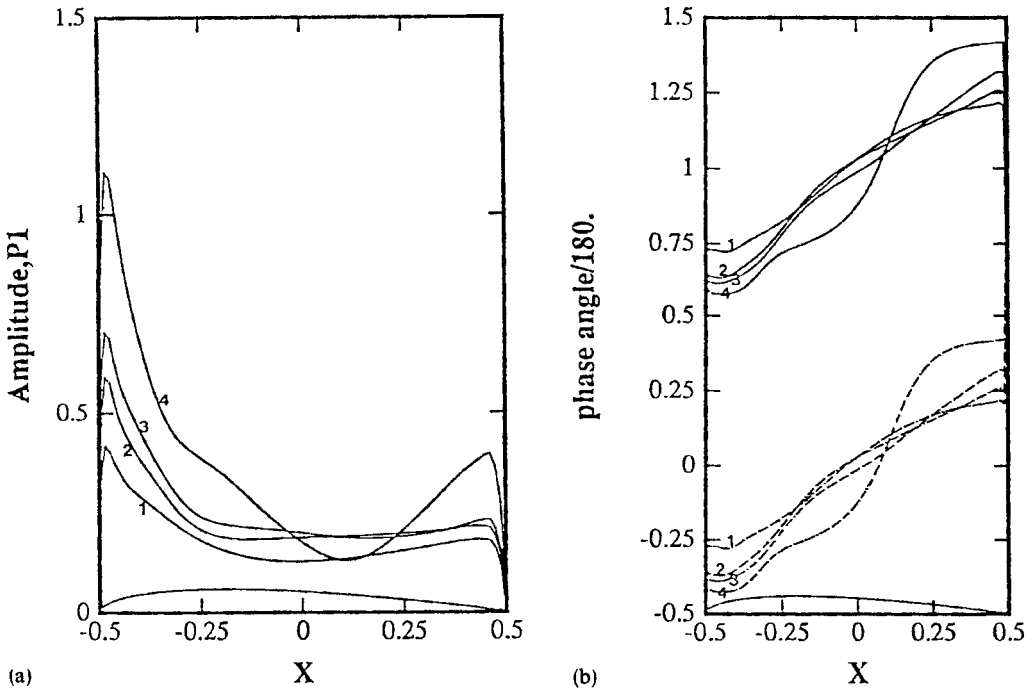

Figure 18. For the first-mode fluctuation for AA I and $M_0=2{\cdot}0$ [(1) $\omega=\pi$; (2) $\omega=2\pi$; (3) $\omega=2{\cdot}5\pi$; (4) $\omega=4\pi$; (——) upper wall; (– – –) lower wall] (a) amplitude; (b) phase angle

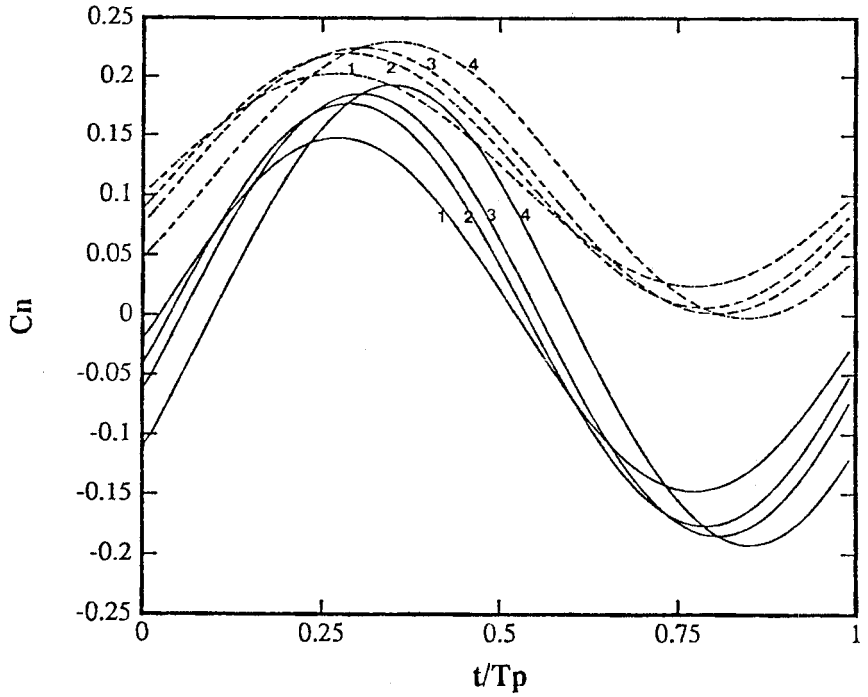

Figure 19. History of normal force coefficient for $M_0=2{\cdot}0$: (1) $\omega=\pi$; (2) $\omega=2\pi$; (3) $\omega=2{\cdot}5\pi$; (4) $\omega=4\pi$; ——, AA I; – – –, AA II

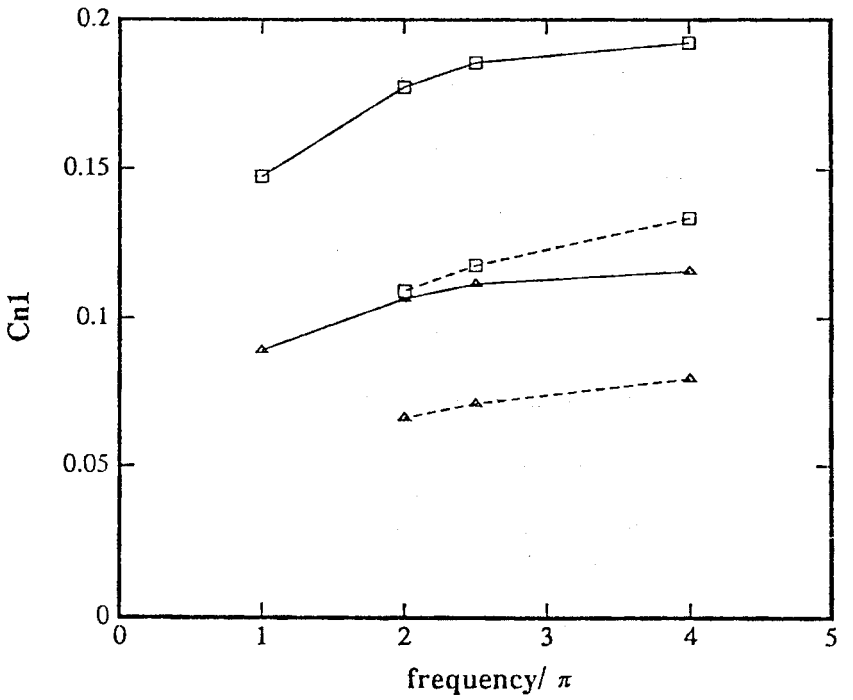

Figure 20. For the first-mode fluctuation of normal force coefficient [(——) $M_0=2{\cdot}0$; (– – –) $M_0=3{\cdot}0$; (□) AA I; (△) AA II]

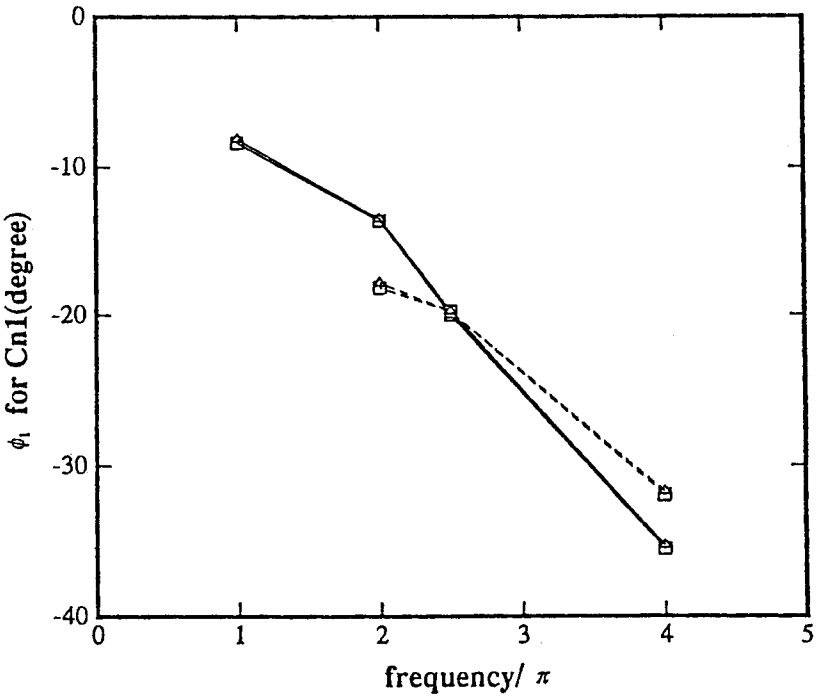

Figure 21. Phase angle of first-mode fluctuation of normal force coefficient [(——) $M_0=2{\cdot}0$; (– – –) $M_0=3{\cdot}0$; (□) AA I; (△) AA II]

APPENDIX: NOMENCLATURE

A, B	Jacobian matrices of E and F
C	sound velocity
C_0	free-stream sound velocity
C_n	normal force coefficient defined by $\int -(P-P_0)ds/0{\cdot}5U_0^2$
C_p	pressure coefficient defined by $-(P-P_0)/0{\cdot}5\,U_0^2$
E, F	flux vectors
J	Jacobian of the transformation
L	characteristic length or aerofoil chord length
P	pressure non-dimensionalized by $\rho_0 C_0^2$
P_0	non-dimensionalized free-stream pressure
P_{steady}	wall pressure of steady flow
P_{wall}	wall pressure of unsteady flow
t	time non-dimensionalized by L/C_0
U, V	contravariant velocity components
U_0	dimensionless free-stream velocity
u, v	velocity components in co-ordinates (x, y) non-dimensionalized by C_0
x, y	Cartesian co-ordinates
x_b, y_b	body axes
ξ, η	general co-ordinates

$\xi_x, \xi_y, \eta_x, \eta_y, \xi_t, \eta_t$	transformation matrices
θ	angle of attack
θ_0	amplitude of oscillating angle of attack
$\theta_1, \theta_2, P_1, P_2$	amplitude of fluctuation
λ	eigenvalue
ρ	density non-dimensionalized by ρ_0
ρ_0	free-stream density
ϕ_1, ϕ_2	phase angle of fluctuation
ω	oscillating frequency

REFERENCES

1. W. F. Ballhaus and P. M. Goorjian, 'Implicit finite difference computations of unsteady transonic flows about airfoils, including the treatment of irregular shock wave motions', *AIAA J.*, **15**, 1728–1735 (1977).
2. R. Magnus and H. Yoshihara, 'Unsteady transonic flows over an airfoil', *AIAA J.*, **13**, 1622–1628 (1975).
3. J. L. Steger, 'Implicit finite difference simulation of flow about arbitrary two-dimensional geometries', *AIAA J.*, **16**, 679–686 (1978).
4. V. Venkatakrishnan and A. Jameson, 'Computation of unsteady transonic flows by the solution of Euler equations', *AIAA J.*, **26**, 974–981 (1988).
5. J. L. Steger and R. F. Warming, 'Flux vector splitting of the inviscid gasdynamic equations with applications to finite-difference methods', *J. Comput. Phys.*, **40**, 263–293 (1981).
6. B. van Leer, 'Flux vector splitting for Euler equations', Lecture Notes in Physics, Vol. 170, 1982, pp. 501–512.
7. J. B. Bell, P. Colella and J. A. Trangenstein, 'Higher order Godunov methods for general system of hyperbolic conservation laws', *J. Comput. Phys.*, **82**, 362–397 (1987).
8. S. Osher and S. Chakravarthy, 'Upwind schemes and boundary conditions with application to Euler equations in general geometries', *J. Comput. Phys.*, **50**, 447–481 (1983).
9. P. L. Roe, 'Approximate Rieman solvers, parameter vectors and difference schemes', *J. Comput. Phys.*, **43**, 357–372 (1981).
10. S. M. Liang and J. J. Chan, 'An improved upwind scheme for the Euler equations', *J. Comput. Phys.*, **84**, 461–473 (1989).
11. L. B. Simpson and D. Whitfield, 'A flux difference split algorithm for unsteady Navier–Stokes solutions', *AIAA-89-1995-CP*, AIAA 9th Comput. Fluid Dynamics Conf., 1989.
12. B. van Leer, J. L. Thomas, P. L. Roe and R. W. Newsom, 'A comparison of numerical flux formulas for the Euler and Navier–Stokes equations', *AIAA paper 87-1104*, AIAA 8th Comput. Fluid Dynamics Conf., 1987.
13. H. C. Yee, 'Construction of explicit and implicit symmetric TVD schemes and their application', *J. Comput. Phys.*, **68**, 151–179 (1987).
14. H. C. Yee, G. H. Klopfer and J. L. Montagne, 'High-resolution shock-capturing schemes for inviscid and viscous hypersonic flows', *J. Comput. Phys.*, **88**, 31–61 (1990).
15. T. H. Pulliam and D. S. Chaussee, 'A diagonal form of an implicit approximate factorization algorithm', *J. Comput. Phys.*, **39**, 347–363 (1981).
16. C. Hirsch, *Numerical Computation of Internal and External Flows*, Wiley, New York, 1988.
17. J. L. Steger and R. L. Sorenson, 'Automatic mesh-point clustering near a boundary in grid generation with elliptic partial differential equation', *J. Comput. Phys.*, **33**, 405–410 (1979).